Modeling and de-embedding the interferometric scanning microwave microscopy by means of dopant profile calibration

L. Michalas, Fei Wang, Charlene Brillard, Nicolas Chevalier, Jean-Michel Hartmann, Romolo Marcelli, Didier Theron

Modeling and de-embedding the interferometric scanning microwave microscopy by means of dopant profile calibration

L. Michalas[1*], F. Wang[2], C. Brillard[2], N. Chevalier[3], J.M. Hartmann[3], R. Marcelli[1] and D. Theron[2]

[1] National Research Council, Institute for Microelectronics and Microsystems (CNR-IMM), Via del Fosso del Cavaliere 100, 00133 Rome, Italy

[2] Institut d'Electronique, de Microélectronique et de Nanotechnologie, CNRS UMR 8520/ University of Lille 1, Avenue Poincaré, CS 60069, 59652 Villeneuve d'Ascq, France

[3] Univ. Grenoble Alpes, F-38000 Grenoble, France and CEA, LETI, MINATEC Campus, F-38054 Grenoble, France.

***** Corresponding Author: Loukas Michalas
email: loukas.michalas@artov.imm.cnr.it
tel: +39 0649934536
fax:+39 0645488066

The paper presents the full modeling and a methodology for de-embedding the interferometric scanning microwave microscopy measurements by means of dopant profile calibration. A Si calibration sample with different boron-doping level areas is used to that end. The analysis of the experimentally obtained S_{11} amplitudes based on the proposed model confirms the validity of the methodology. As a specific finding, changes in the tip radius between new and used tips have been clearly identified, leading to values for the effective tip radius in the range of 45 nm to 85 nm, respectively. Experimental results are also discussed in terms of the effective area concept, taking into consideration details related to the nature of tip-to-sample interaction.

Manuscript

Characterization at the nanoscale, requires new experimental techniques able to provide high resolution and sensitivity. Scanning microwave microscopy (SMM) is a technique which strives to achieve both requirements, offering localized characterization. This is obtained by combining microwave measurements with probe techniques. The operation principle is based on the application of a microwave signal through a tip. Its edge can thus be considered as a microwave source in proximity to the material under investigation. Several configurations of microwave

microscopes have been proposed to that end[1-13]. The gained knowledge is summarized in several reviews [14,-16]. Beside the proper instrumentation setup, a trustworthy calibration and the right de-embedding methodology are equally important in order to extract quantitative information from the experimentally obtained microwave signals. Microwave microscopes provided precise characterization of different types of samples such as dielectrics [17,18], semiconductors [19,20], nano-devices [21-23] , novel/advanced materials[24,25] and biological samples [26].

One of the more recent SMM setups is based on the combination of an atomic force microscope (AFM) with a vector network analyzer (VNA). This setup aims to take advantage of the high lateral AFM resolution and the sensitivity offered by the VNA, if properly connected. A VNA sensitivity is optimum when operating with a load in the order of 50 Ω. Therefore, to take full advantage of the instrumentation capability, the high impedance of the tip/sample system should be matched to the instrumentation impedance [21]. A quite effective configuration calls upon an interferometric setup, thereby offering sub-fF sensitivity for a wide range of capacitances [13] and allowing aF-scale sensitivity [22].

Semiconductor characterization at the nm scale has attracted huge interest in recent years. The corresponding calibration schemes (reported for the setup with a resistor/resonator matching [9]), is based on controlled doping profiles. Calibration is achieved by correlating the derivative of the reflection coefficient amplitude (dS/dV) [27-29] or phase (dP/dV) [30] measured on areas of accurately defined doping, to the corresponding doping level. As recently demonstrated, SMM calibration can also be achieved by the indirect correlation between the doping level and the S_{11} amplitude through the formed metal oxide semiconductor (MOS) capacitance [31]. Given the importance of SMM for nanoscale semiconductor device characterization and the ability of silicon technology to provide structures with accurately defined properties, dopant profile calibration is a very useful tool towards quantitative SMM measurements. Moreover, no such study has been reported before for the interferometric SMM setup.

A dopant profiling calibration study for interferometric SMM is detailed thereafter. The calibration is based on the recently reported approach for correlation of the reflection coefficient amplitude, $|S_{11}|$ to the MOS system capacitance [31], including the concept of effective area [32]. An analytical model for interferometric SMM system is initially presented. The S_{11} amplitude is experimentally obtained on a specially designed calibration sample (with a boron-doping “maya-like” pyramid inside Si) and analyzed according to the proposed model. The analysis leads to a straightforward experimental calculation of all the important quantities for the interferometric setup including also the effective tip radius.

In the interferometric setup of the SMM, the signal coming out of the VNA is divided by a splitter in two. The first part (path 1 (a) – Fig.1) is sent to the device under test (DUT) through the AFM tip, while the second part (path 2 - Fig. 1) goes through an attenuator. The reflected part of the first signal portion (path 1 – Fig.1), coming back from the tip/sample system interaction, is superimposed to the second part, which is adjusted to create a destructive interference at a given reference impedance. These two arms are different in length (about 1 m) so that the interference occurs approximately every 100 MHz. Implementation of a phase shifter, not added in the present setup, would allow also finer adjustment if required. The sum of the signals is also amplified by a factor G in order to enhance sensitivity. This operation principle is presented in Figure 1 and expressed in terms of equations as follows.

The signal $a_{in}=Ae^{i\omega t}$, with an amplitude A and with $\omega = 2\pi f$, f being the frequency, comes out of the VNA source, goes through a splitter and is divided into two equal parts. Those two signals can be expressed at a point x from the source and at time t, as $a_i(x,t) = a_0 e^{-i(kx-\omega t)}$, with $a_0 = A/2$ and $k = 2\pi/\lambda$ (λ being the wave length).

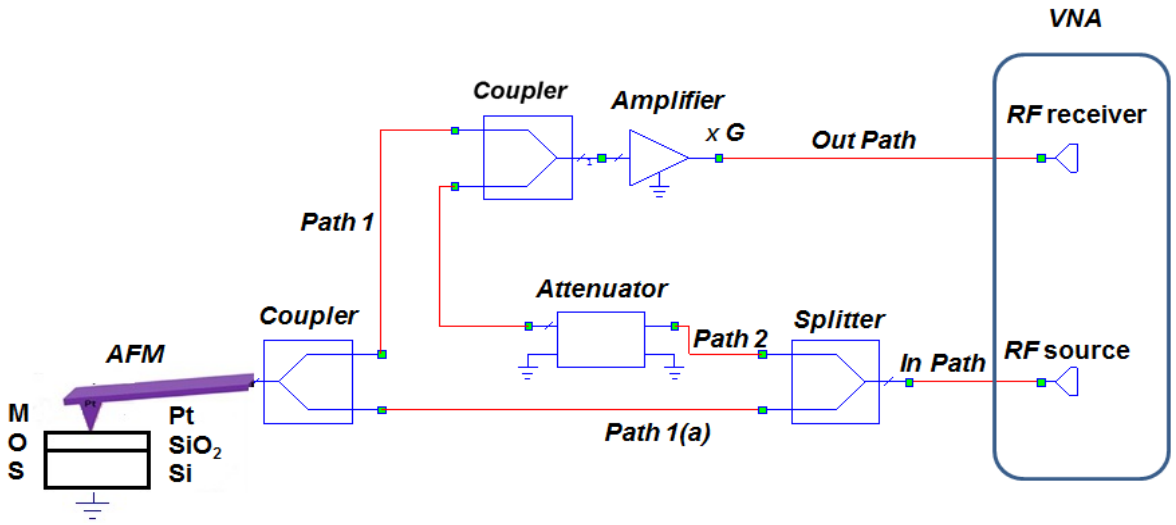

FIG.1 Simplified schematic of the interferometric SMM operation principle

The reflected signal coming out from the tip and the DUT system is

$$a_1(x,t) = e_{10}\Gamma a_0 e^{-i(kx-\omega t)} \quad (1)$$

where Γ is the DUT reflection coefficient and e_{10} reflects the signal attenuation due to propagation in the cables and losses in the splitter and the couplers.

The second part that goes through the attenuator is

$$a_2(x,t) = e_{20}a_0e^{-i(kx-\omega t)} \tag{2}$$

where again e_{20} has a similar meaning than e_{10} but for the second path and includes also the signal adjustment as explained below.

The total signal coming back to the VNA (out path – Fig.1) is the sum of the reflected part of the signal through path 1 and the signal through path 2, amplified by a factor G.

$$a_{out} = Ga_0\left(e_{10}\Gamma e^{-ikx_1} + e_{20}e^{-ikx_2}\right)e^{i\omega t} \tag{3}$$

The signal in path 2 is then adjusted at reference impedance with the reflection coefficient Γ_0 and at a given frequency corresponding to k_0, in order to completely cancel the output and have some destructive interference where $a_{out}=0$.

In that case

$$e_{20}e^{-ik_0x_2} = e^{i\pi}e_{10}e^{-ik_0x_1}\Gamma_0 \tag{4}$$

while the measured S_{11}, defined as $S_{11}=a_{out}/a_{in}$, at any point of the sample and at any frequency will be written as

$$S_{11} = Ge_{10}e^{-ik_0x_1}\left(\Gamma e^{-i(k-k_0)x_1} - \Gamma_0 e^{-i(k-k_0)x_2}\right) \tag{5}$$

Initially a scan versus frequency at the reference impedance with reflection coefficient Γ_0 is performed. In that case, the reflection coefficient will be

$$S_{11-\Gamma_0}(k) = Ge_{10}\Gamma_0 e^{-ik_0x_1}\left(e^{-i(k-k_0)x_1} - e^{-i(k-k_0)x_2}\right) \tag{6}$$

The last equation can be rewritten by implementing trigonometric formulas as

$$S_{\Gamma_0}(k) = 2iGe_{10}\Gamma_0 e^{-ik_0x_1}\sin\left[-\frac{(k-k_0)(x_1-x_2)}{2}\right]e^{-i\frac{(k-k_0)(x_1+x_2)}{2}} \tag{7}$$

Therefore working versus frequency this corresponds to a maximum value for the amplitude equal to

$$\left|S_{11-\Gamma_0}\right|_{max} = |2Ge_{10}\Gamma_0| \tag{8}$$

It is worthwhile to notice that the latter relationship is useful to estimate the effective multiplying factor G.

Then, the frequency is fixed at a value f not far from f_0, and the DUT is scanned. The reflected signal is now coming out from different impedances, with respect to the reference one. In this case, which represents SMM operation, by using $2\pi f = kv_g$, S_{11} is expressed as

$$S_{11-f}(\Gamma) = Ge_{10}e^{-\frac{i2\pi f}{v_g}x_1}(\Gamma - \Gamma_1) \quad (9)$$

$$\text{where} \quad \Gamma_1 = \Gamma_0 e^{-\frac{2i\pi(f-f_0)(x_2-x_1)}{v_g}}$$

Then, if we name $A = Ge_{10}e^{-\frac{i2\pi f}{v_g}x_1}$ and B = -AΓ_1, equation (9) can be written as $S_{11\text{-}f}(\Gamma) = A\Gamma + B$

In the case of small admittances, such as those formed by an AFM tip and the sample, having mainly capacitive contributions, as in the case of MOS structures discussed in this paper, the last equation can be finally written as [8]

$$S_{11-f}(C) = -2iZ_0A\omega(C - C_1) \quad (10)$$

In the last equation Z_0 = 50 Ω, C is the capacitance that is formed by the tip/sample system at the point of measurement and C_1 includes any offset with respect to zero due to any experimental reason. Finally, A can be estimated by the maximum value of the interference versus frequency as expressed in Eq. (8). This equation is the one that will be used for the calibration and de-embedding in the following experimental procedure.

The experimental setup is composed of a Keysight´s E8363B Vector Network Analyzer (VNA) interfaced with a Keysight´s LS5600 atomic force microscope (AFM) with commercially available platinum tips especially designed for SMM measurements, (Rocky Mountain Nanotechnology 25Pt300A [33]) having a spring constant of 18 N/m. In addition and in order to use the interferometric SMM approach, the experimental setup includes also a modified nosecone without any integrated resistor/resonator system, as well as a Mach-Zehnder interferometer. The interferometer consists of a coaxial power divider and two coaxial hybrid couplers associated to an active variable attenuator. The operation principle is presented by the simplified schematics in Figure 1. A detailed description can be found in Ref. [13]. Humidity and temperature were carefully controlled in order to minimize their influence on measurements.

A special calibration sample has been fabricated and cross-sections prepared to perform a dopant profile calibration for interferometric SMM. An Epi Centura™ reduced pressure – chemical vapor deposition (RP-CVD) industrial cluster tool from Applied Materials was used to grow (at 950°C, 20 Torr thanks to SiH_2Cl_2 + HCl + B_2H_6) nine 400 nm thick

layers with well-defined boron doping levels (Fig. 2) on a slightly p-type (10^{15} cm^{-3}) boron doped [~7-10 Ω·cm] Si(001) substrate[34] . The doping levels were measured elsewhere by secondary ion mass spectroscopy (SIMS). The top surface is covered by a roughly one micron thick intrinsic epitaxial silicon layer. The sample presents a symmetric structure around the central layer with similar doping densities on each side (hence our "maya pyramid" denomination).

# Area	9	8	7	6	5	4	3	2	1
Doping (cm^{-3})	4.96 x 10^{17}	1.71 x 10^{18}	4.4 x 10^{18}	1.1 x 10^{19}	4.16 x 10^{19}	1.109 x10^{19}	4.38 x 10^{18}	1.55 x 10^{18}	4.88 x 10^{17}

FIG.2 Schematic representation of the calibration sample. The boron-doping level is extracted from SIMS depth profiling.

The dopant profile calibration methodology is based on the modeling presented above and the recent approach for SMM study of MOS systems based on the concept of the effective area [32]. More precisely and based on Eq. (10), the measured amplitude of the reflection coefficient in the interferometric setup is

$$|S_{11}| = 2Z_0 A\omega |C - C_1| \tag{11}$$

In that case, the tip in contact with the semiconducting sample having a native oxide on top forms a MOS capacitance. The MOS capacitance is quite accurately defined for any doping level as C = (*effective scanned area*) x C_{MOS} where C_{MOS} is the inversion capacitance per unit area defined as [35]

$$C_{MOS} = \frac{\varepsilon_{ins}}{d_{ins} + \frac{\varepsilon_{ins}}{\varepsilon_{sem}} W} \tag{12}$$

Where W is the depletion layer width equal to

$$W = \sqrt{\frac{4\varepsilon_{sem} KT ln\left(\frac{N_A}{n_i}\right)}{q^2 N_A}} \tag{13}$$

In the above equations, ε_{ins} and ε_{sem} are the oxide and silicon dielectric permittivities respectively, d_{ins} is the oxide thickness, K the Boltzmann constant, T the absolute temperature, q the fundamental charge quantity. N_A and n_i are the doping level and the intrinsic carrier concentration, respectively. The native oxide thickness typically saturates around 1 nm [37]. Slight variations around this value, depending on silicon or environmental details, remain negligible before $\frac{\varepsilon_{ins}}{\varepsilon_{sem}} W$. The native oxide thickness was therefore supposed to be constant at 1 nm. Equations (11), (12) and

(13) clearly reveal the indirect relationship between the measured amplitude and the doping level. A linear relationship is expected when plotting the measured $|S_{11}|$ versus the MOS system capacitance C_{MOS} (calculated for any doping thanks to (12) and (13)). If the coefficient A in (11) is known, the slope will yield the effective scanned area and thus the effective tip radius.

Following the procedure explained before, the AFM tip is initially placed in contact at a point of the DUT. This point acts as the reference impedance, Γ_0. The measured signal at the reference point is expected to vary with the frequency as described in (6). The experimentally obtained result is presented in figure 3.

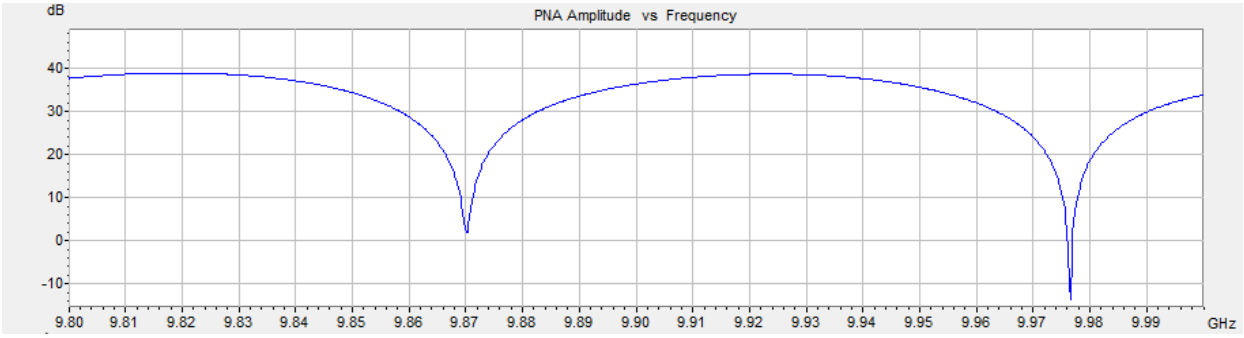

FIG.3 Experimentally obtained interference scheme

This first experimental step is important for the proper application of the following quantitative analysis. Indeed, the gain G and consequently the constant A in equation (10) can be calculated from the maximum value of the interferometer scheme amplitude (Fig.3) versus frequency (as demonstrated in equation (8)). This is of major importance for the accurate estimation of the effective scanned area. In addition, this first experimental step also reveals the most appropriate frequency for the following experimental procedure [13]. In our case, the frequency was fixed at 9.976 GHz.

Different areas were scanned while keeping the RF signal frequency fixed and the AFM tip always in contact with the sample surface. A typical image for the measured amplitude obtained on the calibration sample is presented in figure 4. Nine stripes corresponding to the different doping levels (Fig. 2) are clearly distinguished by color scale differences. The very bright areas at the edges of the sample correspond to the wafer substrate doping level. They were not used in the calibration procedure that follows.

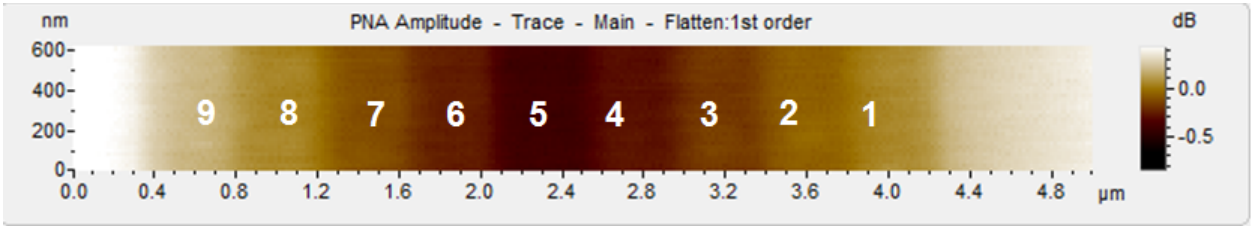

FIG.4.The nine areas with different doping levels in the sample cross-section are clearly visible thanks to the color scale.

Although the different areas are clearly separated, a DC bias was also applied through the AFM tip, using a bias tee in order to perform a quantitative analysis (in conjunction to the microwave signal applied for SMM assessment). The DC signal was used to have MOS inversion at the oxide / semiconductor interface. Indeed, the calibration sample is boron doped (e.g. p-type) silicon while the tip was platinum. Such a combination may lead, in the absence of a DC bias, to different interface conditions depending on the native oxide's electrical charging state and on the properties of the native oxide / Si:B interface.

The proposed calibration was performed using point by point measurements on the different stripes in order to avoid extended charging of the native oxide that would influence measurements. Measurements were carried out twice. Initially, a very fresh tip was utilized. It was used to scan the calibration sample from area 1 to area 5 and then from area 5 to area 9. This way, it is possible to obtain two calibration lines in two different areas with almost the same doping levels. The AFM tip was then enlarged, by continuous use under a contact force of a few µN, and the measurements repeated. The ability of the proposed calibration to identify tip radius changes is thus also evaluated. The experimentally obtained results are presented according to the proposed modeling (equation (11)) in Figure 5.

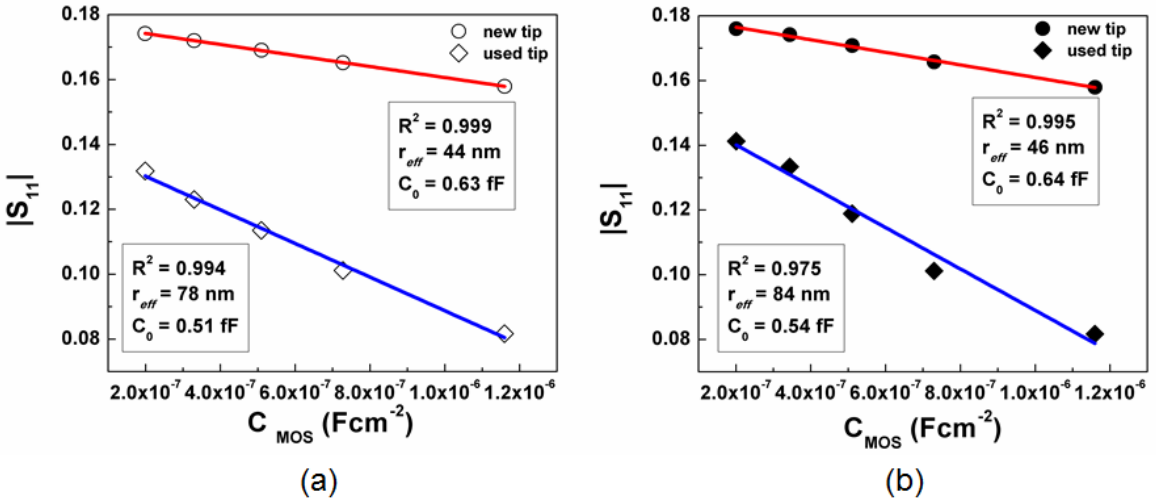

FIG.5 Experimental results and analysis with new or used tips on the calibration sample areas (a) (1) to (5) and (b) (5) to (9). In the legends, R is the linear regression's fitting coefficient process and r_{eff} the estimated effective tip radius.

In all of the above presented configurations, the experimental results obeyed and confirmed the proposed linear relation (11) obtained by the current modeling of the interferometric system. Based on the linear regression process, the effective tip radius derived from the *effective area* by supposing that it is equal to πr_{eff}^2, is calculated from the fitting line's slope. In addition, the quantity C_1 is also obtained by the intercept.

The calculated tip radius is found to increase from 44 nm up to 46 nm (new tip) and from 78 nm up to 84 nm (used tip), respectively, as the time of use increases, which is something expected for contact mode experiments. Indeed, the tip apex is expected to be wearied and/or flattened by direct contact with the sample surface as demonstrated [28]. The fact that the calculated tip radius gradually increases verifies the validity of the proposed modeling and supports the use of the proposed methodology for calibrating and de-embedding interferometric SMM measurements. It is also interesting to notice that the corresponding "skin depths" (e.g. the penetration depths of microwaves) in boron-doped silicon, calculated by using the standard conversion between resistivity and doping [36], are in the range of 25 μm to 130 μm at 10 GHz. They thus should not affect the obtained results. Nevertheless, it should be highlighted that the effective radius may be determined by taking into account the properties of the material under investigation.

Let us now discuss the concepts of effective area (πr_{eff}^2) and tip radius (r_{eff}), initially introduced in [Ref 9] and recently used in Ref. [32] with the appropriate modeling for the resistor/resonator setup. Those are not strictly speaking geometrical quantities. The effective tip radius is indeed representing the actual experimental resolution. It is different

from the nominal geometrical radius (for SMM tips (20nm, typically[33]), as it takes into account interactions away from the contact point between the tip apex and the DUT. Therefore, the effective area is likely to be higher than the geometrical one, as it also incorporates contributions from fringing fields around the tip apex and from the water meniscus. The effective area concept presented here accounts for the wearing of the tip due to the experimental procedure, however. It thus yields an experimental resolution value even in cases where, due to prolonged use, the tip apex shape is not any more the nominal one. The proposed methodology provides also an easy and straightforward experimental way of calibrating experimental results even during the experimental procedure in order to include any small changes that could possibly take place, thereby enhancing measurement accuracy. Moreover, calculations are performed in the contact mode and at a specific operation frequency. These quantities may also affect the effective interaction depending on the specific characteristics of the DUT. Incorporating on wafers such calibration structures in order to determine the effective scanned area during measurement might be most interesting. Finally, C_1 is practically unaffected during the experimental procedure. The calculated values, in the range of sub-fF, are also consistent with the interferomeric concept which minimizes the parasitic capacitances by the formation of destructive interferences using a reference point on the DUT.

In conclusion, a de-embedding methodology for interferometric scanning microwave microscopy is presented which is based on a tailored-made doping profile. To that end, a calibration sample (with a “maya-like” pyramid of boron inside Si) was fabricated. The proposed methodology includes a full system analytical modeling and its application in the case of impedances with mainly capacitive contributions (such as the MOS-type calibration sample under investigation). Experimental results have been analyzed using the concept of effective area/radius that allowed the straightforward experimental determination of the SMM actual resolution. The validity of the proposed model has been evaluated thanks to the use of new or purposely enlarged tips. Changes in the tip radius were clearly identified. The results support the use of the proposed methodology as a useful characterization tool in order to provide an improved accuracy when using interferometric SMM.

Acknowledgement

The authors wish to acknowledge the support from EC by means of “Marie Curie” fellowship in the framework of PEOPLE-2012-ITN project: Microwave Nanotechnology for Semiconductor and Life Science -

NANOMICROWAVE, under GA: 317116, as well as the Region Nord-Pas-de-Calais for supporting this work under the project CPER CIA research and the National Research Agency (ANR) under the program Equipex (EXCELSIOR project).

References

[1] S.J. Stranick and P.S. Weiss, J. Phys. Chem. **98**, 1762 (1994).
[2] C.P. Vlahacos, R.C. Black, S.M. Anlage, A. Amar and F.C. Wellstood, Appl. Phys. Lett. **69**, 3272 (1996).
[3] D.E. Steinhaer, C.P. Vlahacos, S.K. Dutta, F.C. Wellstood and S.M. Anlage, Appl. Phys. Lett. **71**, 1736 (1997).
[4] M. Tabib-Azar, D.P. Su, A. Pohar, S.R. LeClair and G. Ponchak, Rev. Scient. Instr. **70**, 1725 (1999).
[5] A. Imtiaz and S.M. Anlage, Ultramicroscopy **94**, 209 (2003).
[6] C. Gao, B. Hu, P. Zhang, M. Huang, W. Liu and I. Takeuchi, Appl. Phys. Lett. **84**, 4647 (2004).
[7] K. Lai, B. Ji, N. Leindecker, M.A. Kelly and Z.X. Shen, Rev. Scient. Instr. **78**, 063702 (2007).
[8] A. Tselev, S.M. Anlage, Z. Ma and J. Melngailis, Rev. Scient. Instr. **78**, 044701 (2007).
[9] H.P. Huber, M. Moertelmeier, T.M. Wallis, C.J. Chiang, M. Hochleitner, A. Imtiaz, Y.J. Oh, K. Schilcher, M. Dieudonne, J. Smoliner, P. Hinterdorfer, S.J. Rosner, H. Tanbakuchi, P. Kabos and F. Kienberger, Rev. Scient. Instr. **81**, 113701 (2010).
[10] M. Farina, A. Lucesoli, T. Pietrangelo, A. Di Donato, S. Fabiani, G. Venanzoni, D. Mencarelli, T. Rozzi and A. Morini, Nanoscale **3**, 3589 (2011).
[11] M. Farina, D. Mencarelli, A. Di Donato, G. Venanzoni and A. Morini, IEEE Trans. Microw. Theor. Techiq. **59**, 2769 (2011).
[12] M. Farina, A. Di Donato, D. Mencarelli, G. Venanzoni and A. Morini, IEEE Microw. Wirel. Comp. Lett. **22**, 595 (2012).
[13] T. Dargent, K. Haddadi, T. Lasri, N. Clément, D. Ducatteau, B. Legrand, H. Tanbakuchi, and D. Theron, Rev. Sci. Instrum. **84**, 123705 (2013).
[14] C. Gao, B. Hu, I. Takeuchi, K.S. Chang, X.D. Xiang and G. Wang, Meas. Sci. Technol. **16**, 248 (2005)
[15] S. M. Anlage, V. V. Talanov, and A. R. Schwartz, Scanning Probe Microscopy (Springer, 2007), pp. 215–253.
[16] A. Imtiaz, T.M. Wallis and P. Kabos, IEEE Microw. Mag. 15, 52 (2014).
[17] V.V. Talanov, A. Scherz, R.L. Moreland and A.R. Schwartz, Appl. Phys. Lett. **88**, 192906 (2006).
[18] K. Lai, W. Kundhikanjana, M.A. Kelly and Z.X. Shen, Appl. Phys. Lett. **93**, 123105 (2008).
[19] G. Gramse, E. Brinciotti, A. Lucibello, S. Patil, M. Kasper, C. Rankl, R. Giridharagopal, P. Hinterdorfer, R. Marcelli and F. Kienberger, Nanotechnology **26**, 135701 (2015).
[20] A. Imtiaz, T.M. Wallis, J.C. Weber, K.J. Coakley, M.D. Brubaker, P.T. Blanchard, K.A. Bertness, N.A. Sanford and P. Kabos, Appl. Phys. Lett. **104**, 263107 (2014).
[21] H. Happy, K. Haddadi, D. Theron, T. Larsi and G. Dambrine, IEEE Microw. Mag. 15, 30 (2014).
[22] F. Wang, N. Clément, D. Ducatteau, D. Troadec, H. Tanbakuchi, B. Legrand, G. Dambrine and D. Théron Nanotechnology **25**, 405703 (2014).
[23] M. Kasper, G. Gramse, J. Hoffman, C. Gaquiere, R. Feger, A. Stelzer, J. Smoliner and F. Kienberger, J. Appl. Phys. **116**, 184301 (2014).
[24] A. Tselev, N.V. Lavrik, I. Vlassiouk, D.P. Briggs, M. Rutgers, R. Proksch and S.V. Kalinin, Nanotechnology, 23, 385706 (2012)
[25] A. Tselev, A. Klein, J. Gassmann, S. Jesse, Q. Li, S.V. Kalinin and N. Balke, Adv. Mat. Interfaces, 2, 1500088 (2015)
[26] Y.J. Oh, H.P. Huber, M. Hochleitner, M. Duman, B. Bozna, M. Kastner, F. Kienberger and P. Hinterdorfer, Ultramicroscopy **111**, 1625 (2011).
[27] J. Smoliner, H.P. Huber, M. Hochleitner, M. Moertelmaier and F. Kienberger, J. Appl.Phys. **108**, 064315 (2010).
[28] I. Humer, C. Eckhardt, H.P. Huber, F. Kienberger and J. Smoliner, J. Appl . Phys. **111**, 044314 (2012).
[29] A. Imtiaz, T.M. Wallis, S.-H. Lim, H. Tanbakuchi, H.-P. Huber, A. Hornung, P. Hinterdorfer, J. Smoliner, F. Kienberger and P. Kabos, J. Appl. Phys. **111**, 093727 (2012).
[30] I. Humer, H.P. Huber, F. Kienberger, J. Danzberger and J. Smoliner, J. Appl. Phys. **111**, 074313 (2012).
[31] L. Michalas, A. Lucibello, C.H. Joseph, E. Brinciotti, F. Kienberger, E. Proietti and R. Marcelli, *In Procceeding of EUROSOI-ULIS, Joint International EUROSOI workshop and International Conference of Ultimate Integration in Silicon,* Bologna, Italy, 26-28 January 2015, edited by IEEE pp. 269-272.
[32] L. Michalas, A. Lucibello, G. Badino, C.H. Joseph, E. Brinciotti, F. Kienberger, E. Proietti and R. Marcelli, *In Proceedings of 45th EuMW, European Microwave Conference*, Paris, France 5-11 September 2015, Edited by IEEE-EuMA, pp. 159-162.
[33] Rmnano.com
[34] F. Gonzatti, J.M. Hartmann and K. Yckache, ECS Trans. **16** (10), 485 (2008).
[35] S.M. Sze, Physics of Semiconductor Device (John Wiley & Sons, NY (1981).
[36] American Soc. For Testing and Mat. F723-99 (1999).
[37] N. Morita, T. Ohmi, E. Hasegawa, M. Kawakami and M. Ohwada, J. Appl. Phys. **68**, 1272 (1990)